ADVANCED FUNCTIONAL MATERIALS
www.afm-journal.de

Smart Design of Fermi Level Pinning in HfO_2-Based Ferroelectric Memories

Lutz Baumgarten, Thomas Szyjka, Terence Mittmann, Andrei Gloskovskii, Christoph Schlueter, Thomas Mikolajick, Uwe Schroeder, and Martina Müller*

How and why the reliability of ferroelectric HfO_2- and HZO ($Hf_{0.5}Zr_{0.5}O_2$)-based memory devices strongly depends on the choice of electrode materials is currently under intense discussion. Interface conditions such as band alignment, defect formation, and doping are recognized as decisive and interrelated parameters, but a unified picture of the physical mechanisms is still missing. Here, two opposite scenarios of band alignment are found in TiN/HZO/TiN and IrO_2/HZO/IrO_2 using hard X-ray photoelectron spectroscopy, revealing on the one hand the conditions for a stable device performance, and the origin of their degradation on the other. As a key difference, TiN electrodes scavenge oxygen from the HZO, while IrO_2 electrodes supply it. Considering the electronic doping limit of HfO_2, a key condition for the stability of ferroelectric devices can be identified: The alignment of the charge neutrality levelwith respect to the metallic Fermi level, which is pinned by the doping limit. Stable device performance can only be achieved for oxygen-deficient HfO_2-based interfaces, where the Fermi level of the metal electrode is close to the conduction band of the ferroelectric insulator. This empirical model explains the fatigue behavior of HfO_2-based capacitors using either oxygen-scavenging TiN or oxygen-supplying IrO_2 electrodes.

1. Introduction

Hafnia-based ferroelectric capacitors (FeCaps) continue their path of success to realizing nonvolatile memories,[1–6] but however, there remains a gap in our knowledge of how the reliability of devices is related to the material properties of the metallic electrodes and the ferroelectric (FE). Recognizing that the interface between the FE insulator and the metal electrode plays a key role, various electrode materials—including metal nitrides (TiN, TaN) and metal oxides (IrO_2, RuO_2)—have recently been investigated to optimize the performance of HfO_2-based FeCaps.[7–9] To date, it has been established that the metal electrodes and FE are interrelated via their interfaces in terms of chemical reactivity and oxygen vacancy concentration—which determine both the static electric potential and the dynamic switching properties of FeCaps.[9,10]

While a certain amount of oxygen vacancies is necessary to stabilize the orthorhombic FE phase in HfO_2 or $Hf_{0.5}Zr_{0.5}O_2$ (HZO), an undesired increase of these defects at the interfaces lead to charge traps, which in turn cause leakage currents and decrease device reliability.[11–14]

Currently, reliability issues such as wake-up and fatigue are associated with an oxygen defect density off an optimal value.[15] In fact, an increased concentration of oxygen vacancies was observed in FeCaps with poor reliability, located at the TiN electrode interface.[16]

Based on the experience with $Pb(Zr,Ti)O_3$ (PZT) devices, it is believed that the use of metal oxide (MO) electrodes, such as IrO_2 or RuO_2, can improve the emergence and distribution of interfacial defects compared to metal nitrides.[17,18] The underlying

L. Baumgarten, T. Szyjka
Forschungszentrum Jülich GmbH
Peter Grünberg Institut (PGI-6)
52425 Jülich, Germany
E-mail: l.baumgarten@fz-juelich.de

The ORCID identification number(s) for the author(s) of this article can be found under https://doi.org/10.1002/adfm.202307120

DOI: 10.1002/adfm.202307120

T. Szyjka, M. Müller
Fachbereich Physik
Universität Konstanz
78457 Konstanz, Germany

T. Mittmann, T. Mikolajick, U. Schroeder
NaMLab gGmbH
Noethnitzer Str. 64a, 01187 Dresden, Germany

A. Gloskovskii, C. Schlueter
Deutsches Elektronen-Synchrotron
Notkestraße 85, 22607 Hamburg, Germany

T. Mikolajick
TU Dresden
01062 Dresden, Germany

idea is that MO electrodes can serve as an oxygen source and thus may actively reduce the oxygen vacancy concentration at the HfO_2 side of the interface. However, this attempt failed: other than expected, the fatigue behavior of IrO_2 and RuO_2-based FeCaps deteriorates compared to using TiN electrodes,[7,8] and the remanent polarization is even significantly reduced during field cycling. This observation suggests an in-depth analysis of the interrelation of interface chemistry and band alignment. In particular, the question arises, whether the metal/HfO_2 interface requires defects for a stable band alignment, which in turn affects the ferroelectric properties. This idea has not yet been considered and will be the main part of this work.

In principle, established semiconductor physics provides all the essential terms for describing ferroelectric interfaces in HfO_2-based FeCaps. In particular, the model of band alignment between metal and insulator energy levels introduced by Bardeen, Cowley, and Sze, the so-called Fermi level pinning (FLP) model, is well suited to determine the electrostatic potential formation.[19–21] On this basis design rules for optimizing the band alignment for specific applications can be established: For example, the band alignment of HfO_2 as high-k gate dielectric replacing SiO_2 demands for sufficient band offsets in relation to the Si band gap to prevent electron or hole injection.[22,23] In memristive capacitor devices, an internal bias field across the insulating layer is required, and, thus, different, asymmetric band alignments at the two adjacent electrodes are mandatory.[24] In FeCaps, on the contrary, a symmetric band alignment of both capacitor electrodes is of critical importance—in order to avoid internal bias fields within the HfO_2. But which would be the ideal band alignment between metal and HZO in FeCaps to stabilize ferroelectricity, both statically and under electrical switching, remains to be unclear.

Tuning the band alignment at M/HZO interfaces means shifting the Fermi levels of metal and insulator with respect to each other. That said, we expand the FLP model by explicitly taking into account i) the (narrow) doping limit of HfO_2 and ii) a chemical oxygen exchange at the metal/HZO interface. While in metals the Fermi level is freely adjustable, in an insulator or semiconductor it cannot be placed freely within the band gap; it is restricted to a certain energy range—this is the well-known doping limit. Above the doping limit, the insulator or semiconductor needs to compensate for the introduction of any additional charges by the formation of defects. Only in this way the Fermi level (EF) remains located within the energy range defined by the doping limit. Within its band gap of 5.8 eV, HfO_2 has a very limited doping range of about $\Delta(E) = 1.3$ eV, as calculated by Robertson et al.[25]

Consideration of the doping limit, oxygen chemical potential, and band alignment leads to a multi-parameter problem for the resulting ferroelectric properties, which generally must be solved by atomic scale calculations. However, the extreme cases of oxygen-poor and oxygen-rich conditions with corresponding electrode materials can be discussed qualitatively. We have attempted to do this in the present work by considering TiN and IrO_2 electrodes as model systems corresponding to the oxygen-poor and oxygen-rich conditions, respectively. To study the interface chemistry and band alignment simultaneously, we used hard X-ray photoelectron spectroscopy (HAXPES), which provides an information depth of up to 30 nm, as required for the investigation of the buried bottom electrode of a FeCap.[26,27]

Using HAXPES, we quantified the band alignment for metal nitride and metal oxide electrodes element—specifically in the model systems TiN/HZO/TiN and IrO_2/HZO/IrO_2. We find that low work-function (WF) metals at an oxygen-poor interface and high work-function metals at an oxygen-rich interface can be considered as stable—both, statically and during switching. Vice versa, low-WF metals at an oxygen-rich and high-WF metals at an oxygen-poor interface require a significant amount of oxygen vacancies or interstitials for a stable band alignment, which in practice destabilize the FE phase. This approach of understanding the FLP effect qualitatively opens up a more systematic access toward optimizing the device reliability of HfO_2-based FeCaps.

2. The Fermi Level Pinning Effect in HfO_2 and HZO

The design of band alignment at the interface between a metal electrode and ferroelectric insulator is a key parameter for controlling the reliability of FeCaps. If the Fermi level (FL) of the insulator is pinned, its alignment with the metal FL for ensuring thermodynamic equilibrium leads to a potential step at the vacuum levels and, hence, a charge transfer across the interface. While the latter is not considered in the simple Schottky–Mott model (and hence fails in predicting band offsets, etc.), charge transfer is included in the improved FLP model presented by Bardeen, Cowley, and Sze.[19,20] However, band alignment is typically treated here as an adjustment of the metal FL relative to fixed insulator energy levels, specifically the charge neutrality level (CNL), as defined below. In the following, we show that the reverse view—that is, assuming a fixed metal Fermi level and adjusting the CNL of the insulator—is particularly useful to target the band alignment of HfO_2 and HZO with different metal electrodes.

2.1. Fermi Level Pinning Model: Basics

Figure 1 illustrates the relevant parameters of the FL pinning effect in the metal-insulator (M/I) band alignment model. The M/I interface is considered as a layer of thickness δ and dielectric properties which are different from the metal and the insulator. Its interface density of states (DOS) at the insulator side is indicated by the striped ribbon. Without referring to specific interface states, like metal-induced gap states (MIGS),[21] a "dead layer" (i.e., a region that is not ferroelectric) at the interface of about 1 nm thickness has been extensively discussed in the case of FeCaps.[28] For the qualitative discussions of the band alignment within this paper, the specific dielectric properties of this layer are not required. In addition to the intrinsic interface states, a defect DOS is indicated by a Gaussian distribution at the energy E_{def}. Both states are considered as an intrinsic and an extrinsic contribution to the band alignment, respectively. These two types of interface states typically possess a CNL (E_{CNL}), which divides its DOS into the same number of states above and below and thus may be considered as the interface FL. Like the bulk FL in semiconductors by doping states, the CNL is also shifted by interface defect states. If E_{CNL} differs from the electrode metal FL

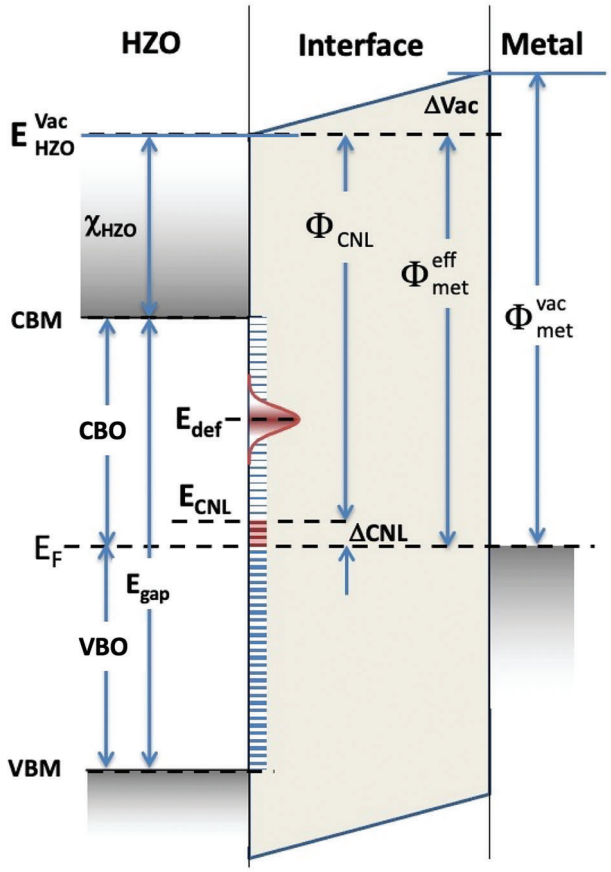

Figure 1. Band alignment at a metal/insulator interface defining the relevant parameters of the Fermi level pinning model.

energy, this results in an imbalance of occupied and unoccupied interface states with a corresponding interface charge density. A proper band alignment is achieved if this interface charge is in accordance with the potential step at the vacuum levels (Δ_{Vac}).

Within the empirical FL pinning model, this accordance condition is easily achieved, if the interface layer is treated as a classical capacitor. The potential step Δ_{Vac} is related to an interface charge Q by the relation $Q = C \cdot U$, with $U = \Delta_{Vac}$ and $C = \varepsilon_r \varepsilon_0 A/\delta$ being the capacitance of the interface layer. The interface areal charge density Q_{int} is then given by

$$Q_{int} = \frac{Q}{A} = \left(\frac{\varepsilon_r \varepsilon_0}{\delta}\right)\Delta_{Vac} \tag{1}$$

Assuming a constant interface DOS D_{int}, at least in the energy region between E_{CNL} and E_F (red-shaded striped ribbon in Figure 1), D_{int} is then given by the difference between FL energy of the metal and the CNL energy of the interface states

$$Q_{int} = e_0^2 D_{int} \cdot \Delta_{CNL} = e_0^2 D_{int} \cdot (\Phi_{met}^{eff} - \Phi_{CNL}) \tag{2}$$

Thus, according to the capacitor Equation (1), the potential difference Δ_{Vac} can be related to Δ_{CNL} by

$$\frac{e_0^2 \cdot D_{int} \cdot \delta}{\epsilon_r \epsilon_0} \cdot (\Phi_{met}^{eff} - \Phi_{CNL}) = (\Phi_{met}^{vac} - \Phi_{met}^{eff}) \tag{3}$$

Table 1. Band alignment parameters of HfO_2 and HZO. Listed are available literature data for the band gap, electron affinity χ, pinning factor S, and calculated charge neutrality level (CNL) as measured from the valence band maximum (VBM).

	HfO_2	HZO
E_{gap} [eV]	5.7–6[30,35–37]	5.2–5.4[8,31,37–40]
Electron affinity χ [eV]	2.2–2.5[35,36,41]	2.2[39]
E_{CNL}-E_{VBM} [eV]	3.64–3.9[22,41,42]	–
FL pinning factor S	0.67–0.7[30,43]	0.8 ± 0.05[31]
$V^{\bullet\bullet}$ E_{def}-E_{CBM} (eV)	0.6–1.2[11,44–47]	

which can be reformulated into the well-known FLP equation[22,29,30]

$$\Phi_{met}^{eff} = \Phi_{CNL} + S(\Phi_{met}^{vac} - \Phi_{CNL}) \tag{4}$$

or, equivalently,

$$\Phi_{met}^{eff} = (1 - S) \cdot \Phi_{CNL} + S \cdot \Phi_{met}^{vac} \tag{5}$$

with the pinning factor S typically given by

$$S = \frac{1}{\left(1 + \left(\frac{e_0^2 D_{int} \delta}{\epsilon_r \epsilon_0}\right)\right)} \tag{6}$$

In **Table 1**, the experimentally known material parameters for HfO_2 and HZO, according to Figure 1 and Equation (4), are listed. The band gap of HZO is reported to be about 0.2–0.4 eV smaller than for HfO_2.[31–33] For the electron affinity, it has to be noted that values of 1.75 and 2.9 eV[34] are reported as well, which are far out of the commonly considered range as tabulated. It also should be pointed out that the published CNLs, as listed, are frequently referenced to the valence band maximum (VBM), whereas Φ_{CNL} in Equations (2) –(6) is referred to the vacuum level (see Figure 1). The energy of the oxygen vacancy $V^{\bullet\bullet}$ defect level E_{def} is referred to the conduction band minimum (CBM).

2.2. Interface Defects as Key Parameter

Since E_{CNL} separates an equal amount of interface states above and below, obviously, it depends not only on the intrinsic interface DOS D_{int}, but also on the extrinsic density of defect states at the interface. Thus, for an equal distribution of interface states in the presence of additional defect states, Φ_{CNL} may be written as

$$\Phi_{CNL} = \Phi_{CNL}^{int} - \Delta\Phi_{CNL}^{def} \tag{7}$$

The shift $\Delta\Phi_{CNL}^{def}$ of the intrinsic CNL has to compensate half of the additional interface defect states N_{def} by the same amount of intrinsic interface states.

$$D_{int} \cdot \Delta\Phi_{CNL}^{def} = 1/2 \cdot N_{def} \tag{8}$$

Following Figure 1, any decrease of the defect density shifts E_{CNL} toward the VBM, while increasing the defect density shifts E_{CNL} toward the CBM. Thus, decreasing the defect density reduces the VBO and vice versa.

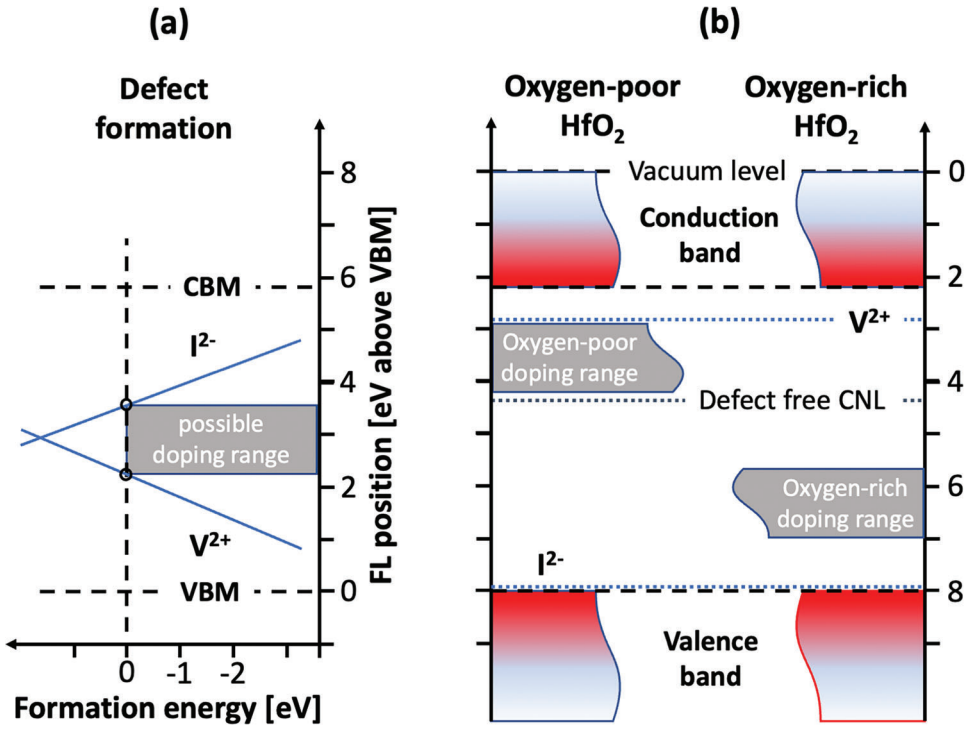

Figure 2. a) Schematic sketch of defect formation energies for oxygen vacancies and interstitials, depending on the FL position (blue lines). Zero energy separates the region of required energy at positive values from energy gain at negative values. Thus, negative formation energies indicate the possibility of spontaneous formation of oxygen vacancies (V^{2+}) or oxygen interstitials (I^{2-}). The doping range without any spontaneous defect formation possibility is highlighted as grey area. The position of this doping range depends on the oxygen chemical potential at the interface.[15,25] b) Doping ranges of HfO_2 under extreme oxygen-poor and oxygen-rich conditions as calculated by Robertson et al.[25,48] The energy scale assumes a band gap of 5.8 eV and an electron affinity of 2.2 eV. Also indicated are the CNL of a defect-free interface, as well as the single particle oxygen vacancy state (V^{2+}) and oxygen interstitial state (I^{2-}) as calculated by Xiong et al.[44] (blue dotted lines).

The band alignment description by the FL pinning model is commonly viewed as an adjustment of the metal FL relative to a given and fixed CNL. However, if the metal FL is fixed to a certain energy by any means, one may also consider the case of a CNL adjustment by defects relative to the pinned metal FL. This will be of particular importance in discussing the IrO_2 band alignment. Experimentally, a defect-free interface is hard to realize—but the defect density might be explicitly tuned by specific processing for a targeted band alignment.

For capacitor-based ferroelectric memories (FeRAMs), a symmetric band alignment of both electrodes is desired to avoid internal bias fields across the ferroelectric layer. But even for a formally symmetric metal–ferroelectric–metal (MFM) structure, the real band alignment at the bottom and top electrodes may be different due to different defect densities induced by layer growth: At the bottom electrode, the subsequent processing of the ferroelectric layer will influence the interface chemistry, whereas this process is skipped for growth of the top electrode.

2.3. Doping Limits of HfO_2 and HZO

Shifting the Fermi level of semiconductors or insulators by doping is one of the main tuning knobs for electronic device design. In general, p-type or n-type doping in semiconductors or insulators results in a downward shift or increase of the VBO at the metal/insulator interface, respectively. However, if the doping concentration reaches a certain level, a further increase of dopants does not result in a further energy shift of the Fermi level: The increase of doping charges is compensated by a spontaneous creation of charged lattice distortions. This is the so-called doping limit, well known for semiconductors and insulators.[25,48] For Si and III–V as well as II–VI semiconductors, the possible doping range energetically covers or even exceeds the full band gap, and in these cases, there is no practical limitation on doping.[49]

For HfO_2, the situation is completely different: According to Robertson et al.,[25] the doping range amounts to only 1.3 eV within the 5.8 eV wide band gap. This range was calculated from the formation energies of the different possible defects in HfO_2 and is schematically shown in **Figure 2**a. For negative energy values, spontaneous defect formation is possible. The doping range indicates the energy range in which no spontaneous defect creation happens. The position of the doping range within the band gap depends on the chemical potential of oxygen which is directly connected to the oxygen concentration.[15,50] In the oxygen-poor case, the doping range is near the CBO, whereas in the oxygen-rich case, it is near the VBM. These two opposite cases, as calculated by Robertson et al.,[25,48,51] are depicted in Figure 2b.

In both cases, any attempt to move the Fermi level out of the doping range would result in the spontaneous creation of defect charges to compensate for the doping charge and keep the

FL within the doping region. These charges would be negative above and positive below the possible doping range. In the case of HfO_2 and HZO, these spontaneously created defects are positively charged oxygen vacancies V^{2+} for a FL energy below the doping range, and negatively charged oxygen interstitials I^{2-} for FL energies above.[50,52]

The doping limits play a crucial role not only for the position of the Fermi level in the bulk HfO_2 and HZO, but also for the band alignment at the interfaces: 1) The metal FL at the interface is always forced into the allowed doping range. 2) The FL pinning condition can only be satisfied by generating additional defect charges and thus shifting the CNL. Since the position of the doping range depends on the chemical potential of oxygen, an exchange of oxygen at the interface is also of particular importance for meeting the FL pinning condition.

The different doping ranges for oxygen-poor and oxygen-rich conditions of HfO_2 and HZO are depicted in Figure 2b, from which we derive different band alignment requirements when using n-type or p-type metals as electrode materials. First, we consider an oxygen-poor condition (Figure 2b, left) for n-type or p-type metals. The band alignment of an n-type metal with a vacuum work function between 4 and 5 eV is easily achieved: Confinement to the doping range creates only a small voltage step at the vacuum level, which can be matched to the CNL within the confined doping range, without introducing further defects. For a p-type metal with a work function between 5 and 6 eV, in contrast, the fixation of the FL in an oxygen-poor range leads to a large potential step at the vacuum level. In this case, the alignment requires a significant shift of the CNL by creating positively charged defects. Second, if we consider an oxygen-rich condition (Figure 2b, right), the same applies with reversed polarity. Attempting to align an n-type metal results in a huge potential step at the vacuum levels and a significant amount of negatively charged interstitials are required, while the FL of p-type metals can be matched to the CNL under oxygen-rich condition with almost no additional defect charges. Thus, the alignment of an n-type metal under oxygen-poor conditions and a p-type metal under oxygen-rich conditions at the interface may be considered as intrinsically stable without the need to create defects. The extreme cases of oxygen-poor and oxygen-rich conditions can be discussed qualitatively, as done in this paper. However, the general case of electrode metals that neither scavenge nor supply oxygen to the interface, like W or Pt, requires further investigation supported by atomic calculation.[53]

3. Experimental Access to Band Alignment

X-ray photoelectron spectroscopy (XPS) provides direct experimental access to the microscopic roots of internal charge distribution and electric fields in solids since the chemical and electronic states of the core and valence levels are recorded element selectively. In addition to surface-sensitive XPS at photon energies between 1 and 2 kV, buried interfaces in real devices are also experimentally accessible using the hard X-ray variant of photoelectron spectroscopy (HAXPES) at photon energies up to 10 kV. Due to the high kinetic energy of core level photoelectrons, the information depth increases up to several 10 nm.[54]

Two effects are essential for the HAXPES analysis of the band alignment, charge distribution, and internal electric fields in

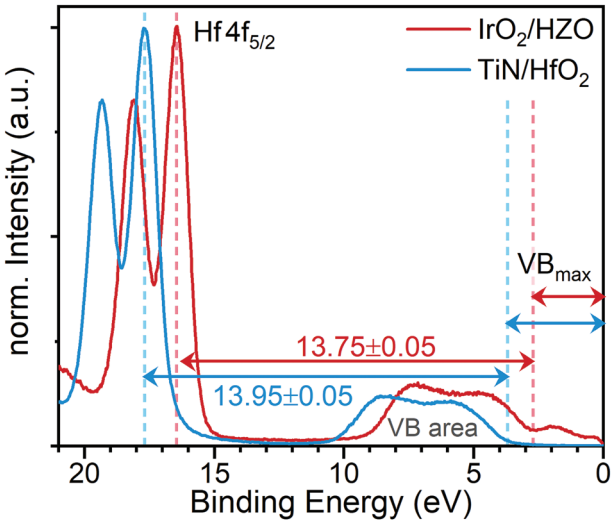

Figure 3. HAXPES photoelectron spectra of IrO_2/HZO (red) and TiN/HfO_2 (blue) samples, which are taken as a reference for the Kraut method (see text). The dissimilar binding energy difference between Hf 4f and VBM at IrO_2/HZO and TiN/HfO_2 indicates a chemical shift of 200 meV, while a rigid binding energy shift is responsible for the different VBMs.

MFM capacitors: First, the so-called rigid binding energy shift, which is caused by a change of the Fermi level position within the band gap of an insulator and shifts all valence bands and all core levels of the insulator by the same value. A rigid core level shift also alters the valence band offset (VBO). Second, the so-called chemical binding energy shift of a core level, caused by a change of the local electronic structure due to chemical bonding. On the contrary to the rigid shift, a chemical shift is individual and different for all core levels; it is caused by a modified screening of core levels and may also reflect interaction with valence electrons.

Both effects are exemplarily shown in **Figure 3** for HAXPES spectra of i) a $Hf_{0.5}Zr_{0.5}O_2$ layer in contact with an IrO_2 bottom electrode and ii) HfO_2 with TiN bottom electrode. The binding energy (BE) scale ranges from the Fermi level up to the Hf 4f core levels. Indicated is the VBM and the binding energy difference between VBM and Hf $4f_{7/2}$. The VBO is equal to the binding energy of the VBM of the metal electrode.

For the IrO_2 bottom electrode, the VBM equals 2.7 eV and shifts to 3.7 eV for the TiN bottom electrode. The same shift of ≈1 eV is observed at the Hf 4f core levels. However, this shift is superimposed by an additional chemical shift, given by the binding energy difference between Hf 4f and VBM: It changes from 13.75 ± 0.05 eV for IrO_2/HZO to 13.95 ± 0.05 eV for TiN/HfO_2. Without this chemical shift, the rigid core level shift can be taken as an indirect measure for the change of the VBO.[55] Different interface charge densities are thus directly accessible by changes of VBOs. This is particularly important for heterostructures, where the observed valence band is generally a superposition of different layers and the VBM of the individual layers is not directly accessible. The rigid core level shift can then be taken as an element and layer specific measure of the VBO change (Kraut method[55]). A prerequisite for this analysis is a constant BE difference between the core levels and VBM without chemical shift. Tracking

Table 2. Valence band offsets (VBOs) experimentally determined by HAXPES for different metal electrodes used as top (TE) and/or bottom electrode (BE) in MFM capacitors. All values refer to the pristine state of the capacitor, with either HfO_2 or HZO ferroelectric layers, which were deposited using PVD or ALD, respectively. The Hf $4f_{7/2}$ binding energy difference to the valence band maximum (VBM) was 13.75 eV for capacitors with IrO_2 electrodes and 13.95 eV for TiN electrodes.

	Capacitor materials			VBO [eV]	
	BE	Ferroelectric	TE	BE	TE
1	$TiN^{(PVD)}$	$HfO_2^{(PVD)}$	$TiN^{(PVD)}$	3.7	3.8
2	$TiN^{(PVD)}$	$HfO_2^{(ALD)}$	$TiN^{(PVD)}$	3.45	–
3	$TiN^{(PVD)}$	$HZO^{(ALD)}$	$TiN^{(PVD)}$	3.45	3.4
4	$TiN^{(ALD)}$	$HZO^{(ALD)}$	$TiN^{(ALD)}$	3.4	–
5	$TiN^{(PVD)}$	$La{:}HfO_2^{(ALD)}$	$TiN^{(PVD)}$	3.5	–
6	$TiN^{(PVD)}$	$Gd{:}HfO_2^{(ALD)}$	$TiN^{(PVD)}$	3.35	–
7	TiN/TiO_2	$HfO_2^{(PVD)}$	$TiN^{(PVD)}$	3.65	–
8	IrO_2	$HZO^{(ALD)}$	IrO_2	2.7	2.55
9	IrO_2	$HZO^{(ALD)}$	Ir	2.7	3.0
10	IrO_2	$La{:}HfO_2^{(ALD)}$	IrO_2	2.25	–

the element-specific chemical BE shifts as well as the rigid BE shifts of all core level peaks, allows identification of charge transfer, redox processes, and band bending at interfaces.[26]

4. Results and Discussion

4.1. Electrode Material-Dependent Valence Band Offsets

In **Table 2** the VBOs of TiN and IrO_2 electrodes are compiled, as experimentally determined from HAXPES spectra according to Figure 1. As explained in the previous section, the analysis is performed either by direct evaluation of the VBM, or indirectly from the Hf 4f core level binding energy shift according to the Kraut method.[55] Values for the bottom and selected top electrodes are listed for HfO_2 and HZO ferroelectric layers, which were grown either by physical vapor deposition (PVD) or atomic layer deposition (ALD), respectively. Also included are the VBOs for an oxidized TiN/TiO_2 electrode as well as HfO_2 layers doped with La or Gd.

For TiN electrodes, VBOs ranging from 3.4 to 3.8 eV are observed, where basically the lower value is obtained for ALD-grown HfO_2 and HZO. Doping with La or Gd has no significant effect on the VBO for TiN electrodes. Within the experimental error, they agree with the lower VBO values of 3.4 eV in the undoped case. The VBO of the TiN top electrodes differs only slightly from the VBO of the bottom electrodes.

For IrO_2 electrodes, in contrast, a VBO range from 2.5 to 2.7 eV is observed, which is about 1 eV smaller than for the TiN electrodes. In contrast to TiN electrodes, the La doping significantly reduces the VBO to 2.25 eV. For a metallic Ir top electrode, prepared by forming gas (FGA) reduction of IrO_2,[56] a VBO of 3.0 eV is observed.

Next, we compare the observed VBO results with the expectations of the FL pinning model. Equation (5) relates the vacuum work function Φ_{vac} of the metal electrode to its effective work function (EWF) at the interface. Assuming a certain band gap and electron affinity, this can be directly related to an expected VBO or CBO (see Figure 1). **Table 3** lists the published values for the Ir, IrO_2, and TiN electrode vacuum work functions, as well as the resulting EWF ϕ_{eff}^{theo} and VBO^{theo}. A FLP parameter $S = 0.7$ and band gaps of 5.8 eV for HfO_2 and 5.4 eV for HZO are used along with an electron affinity $\chi = 2.2$ eV. Due to the reduced band gap of HZO, the CNL Φ_{CNL} is assumed to be slightly scaled down from 3.6 eV above VBM in HfO_2 to 3.4 eV in HZO. The given range of the theoretical VBOs reflects the spread of the published vacuum work functions. The reported wide work function range of Ir results from different orientations of the single crystal surface. For poly crystalline Ir a value of 5.25 eV is reported.[57]

Table 3. Published vacuum work functions of Ir, IrO_2, and TiN as referenced. Theoretical effective work functions are calculated by Equation (5) with an assumed pinning factor $S = 0.7$, a band gap of 5.8 eV for HfO_2 and 5.4 eV for HZO an electron affinity of 2.2 eV and a charge neutrality level of 3.6 eV for HfO_2 and 3.4 eV for HZO.

	Ir(HZO)	IrO_2(HZO)	TiN(HfO_2)	TiN(HZO)
Φ_{vac}	5.25–5.97[57,58]	4.23[59,60]	4.2–4.5[61]	
ϕ_{eff}^{theo}	4.9–5.4	4.2	4.25–4.45	4.2–4.4
VBO^{theo}	2.2–2.7	3.4	3.55–3.75	3.2–3.4
VBO^{exp}	3.0	2.55–2.7	3.4–3.8	3.4

Comparison of expected and observed VBOs, as listed in Table 3, shows that the experimentally observed VBOs of TiN are clearly within the expected range of the FL pinning model, and the observed value for Ir is also close to it. The VBO for IrO_2 is definitely outside the expected range. Based on their vacuum work functions, IrO_2 and TiN are expected to behave similarly. In case of IrO_2 it should also be noted that almost identical VBOs were recently published by Chernikova et al. for RuO_2 electrodes.[8] This seems surprising since the vacuum work functions differ significantly (see discussion below). Both IrO_2 and RuO_2 have been discussed as possible oxide electrodes that have the potential to improve the reliability of HfO_2-based capacitors.

In the following sections, we will discuss the VBOs of these electrode materials in terms of oxygen vacancies and interstitials, doping, the role of oxygen exchange at the interface, and the influence of ferroelectric switching on band alignment.

4.2. Band Alignment for TiN Electrodes

TiN is currently the most relevant electrode material for HfO_2-based FeCaps, although several reliability issues are related to properties at its interface, most notably oxygen scavenging and the resulting increased defect concentration.[16] Several attempts have been made to stabilize the TiN interface and reduce the defect concentration.[62,63] However, a detailed microscopic understanding of the reliability issues associated with the TiN is still pending.

4.2.1. HAXPES Analysis of VBOs

Figure 4 shows Hf 4f spectra with similar TiN bottom electrode but differently grown HfO_2 or HZO. From (a)–(c), Hf 4f spectra from sample numbers 1, 2, and 4 of Table 2 are depicted.

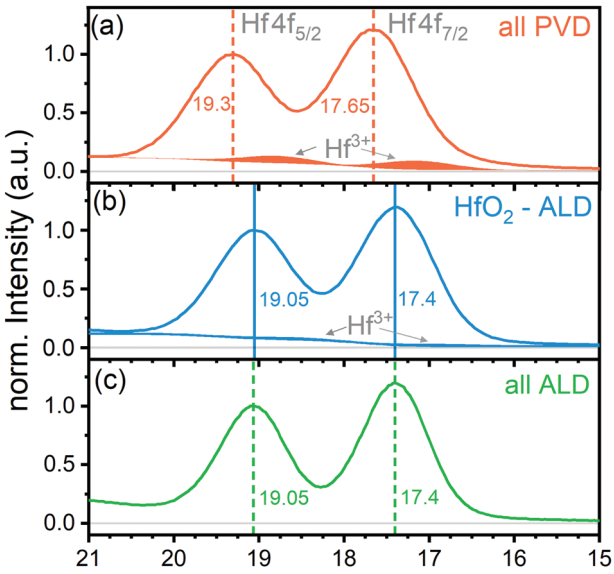

Figure 4. HAXPES Hf 4f core levels rigid binding energy shifts for samples with TiN bottom electrodes and different growth methods for HfO_2, HZO, and TiN. A Hf^{3+} component is observed for a) PVD-grown and b) ALD-grown HfO_2, which is not present in the completely ALD-grown sample (c). Hf^{3+} is typically interpreted as an indirect sign for the existence of oxygen vacancies.[62,64]

Depending on the sample growth method, the spectra show a rigid shift toward lower binding energies, that is, 17.65 eV for the PVD-grown sample and 17.4 eV for the ALD-grown ferroelectric layers. The binding energy is directly correlated with the VBO of the samples as listed in Table 2 (see Figure 3). A larger VBO of 3.7 eV is observed for capacitors which are completely PVD-grown and smaller VBOs of 3.4 eV for ALD-grown capacitors. The choice of HfO_2 or HZO as ferroelectric material seems to be of minor importance for the VBO. However, due to the smaller band gap for HZO, the same VBO leads to a lower EWF for HZO (see **Figure 5**).

In addition to the Hf^{4+} spin–orbit doublet, the spectrum of a fully PVD-grown sample in Figure 4a consists of an additional doublet, related to Hf^{3+}, which has been analyzed in detail in previous publications.[16,62,64] This contribution almost disappears in (b) and completely in (c). The Hf^{3+} component is commonly associated with the presence of oxygen vacancies, which are considered to be the most relevant point defects in HfO_2-based ferroelectrics. If an oxygen vacancy is created by removing a neutral oxygen atom, two excess electrons remain at the lattice site. If these two electrons are transferred to two Hf sites, the vacancies are indirectly detectable by the chemically shifted Hf^{3+} component in the HAXPES Hf 4f spectra ($Hf^{4+} + e^- \rightarrow Hf^{3+}$). Importantly, the spectral disappearance of the Hf^{3+} component does not necessarily indicate a reduction of the defect density. For example, a neutral or negatively charged vacancy will not give rise to an Hf^{3+} component.[64]

The VBO and thus the band alignment at the TiN electrode interface appears to be limited to a VBO range between 3.4 and 3.8 eV. Even a cation doping by La^{3+} or Gd^{3+} does not reduce the VBO (samples 5 and 6). To understand this behavior, we mainly consider four observations:

(i) The calculated energy of the (CNL of a defect-free HfO_2 interface is nearly equal to the FL position of TiN when both vacuum levels are aligned.
(ii) It is known that TiN electrodes scavenge oxygen from HfO_2, forming TiN_yO_x at the interface and an increased oxygen vacancy density in HfO_2.[16]
(iii) The increased oxygen vacancy concentration by oxygen scavenging creates an oxygen-poor condition on the HfO_2 side of the interface.[52]
(iv) The calculated doping range of HfO_2 under oxygen-poor conditions ranges from about 3.5 to 4.8 eV above the VBM, with the lower doping limit also nearly coinciding with the CNL.

Considering these four points, Figure 5 shows the observed band alignment of samples 2 and 3 in Table 3, taking into account the uncertainty of the experimental values of the TiN vacuum work function, the assumed band gap of HfO_2 (5.8 eV) and HZO (5.4 eV) and the assumed electron affinity (2.2 eV). The energy of the doping range and the CNL depends on the calculation method. Therefore, the small potential steps at the vacuum level as well as the energy difference between FL and CNL depend crucially on these values, especially due to their close agreement. However, these uncertainties do not affect the discussion and conclusions drawn below.

Band alignment is achieved with an FL at the lower boundary of the doping range without a significant charge transfer across the interface. In this case, the number of charged defect states at the interface becomes a decisive factor for fine-tuning the band alignment. The single particle states for positively charged vacancies are obtained near the CBM[44] (see Figures 1 and 2b). Thus, an increased amount of oxygen vacancy defect states at the interface shifts the energy position of the CNL E_{CNL} up toward the CBM. Consequently, according to Equation (5), the EWF (Φ_{met}^{eff}) decreases and the VBO increases for an appropriate band alignment. Accordingly, the interface defect concentration in PVD-grown capacitors should be higher than in ALD-grown ones, which is in agreement with the observed decrease of the Hf^{3+} in ALD prepared HfO_2 films since the Hf^{3+} component in the Hf 4f spectra is an indication for oxygen vacancy defects.[64] Thus, the observed change of the VBO from fully PVD-grown samples to fully ALD-grown samples can be conclusively explained by a reduction of oxygen vacancy defect states associated with different growth methods of the capacitor stack.

4.2.2. Impact of La and Gd Doping

In general, a reduction of the VBO could be expected from cation doping with lower valence elements compared to Hf^{4+}. In addition to stabilizing the ferroelectric state by lattice distortion, the most promising cation doping elements (La, Gd) act also as hole dopant elements, due to their formal 3+ valency compared to 4+ of Hf.[65] The FL and CNL at HfO_2 should be shifted toward the VBM and the VBO of the band alignment should be reduced by these elements. As listed in Table 2, the VBO of La- and Ga-doped ALD-grown HfO_2 also were investigated (sample nos. 5 and 6). Compared to the undoped case of sample 2, the VBOs for La- and Gd-doped samples are similar within the estimated error range. Therefore, La or Gd doping does not lead to a

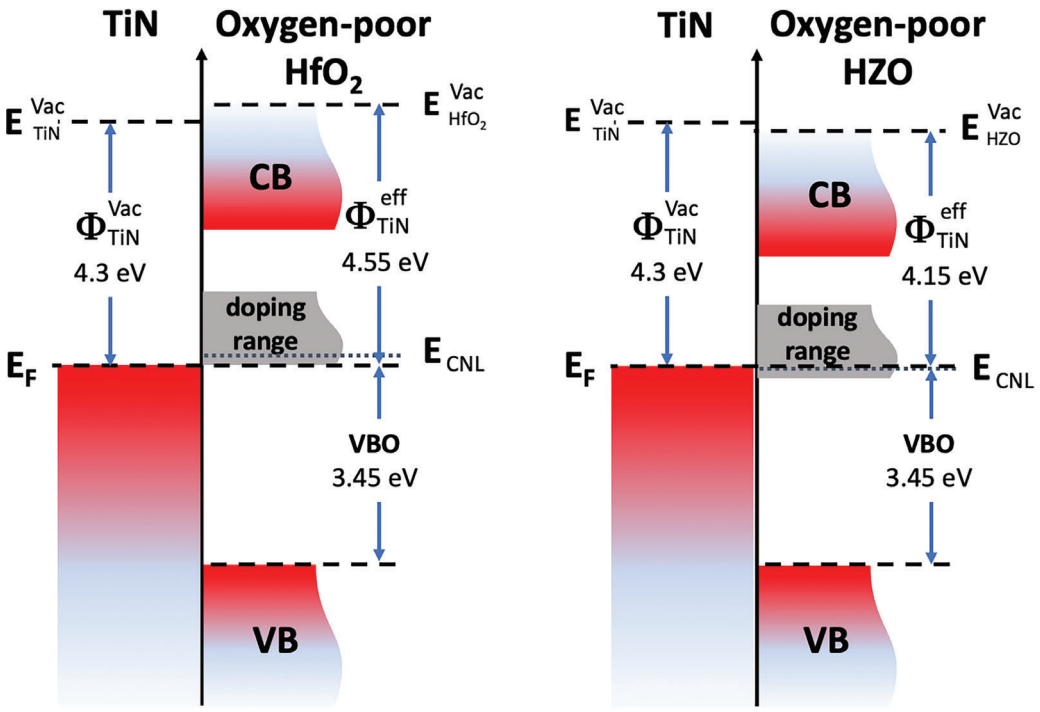

Figure 5. Schematic sketch of TiN band alignment at interfaces to a) HfO_2 and b) HZO. Although the observed VBO is the same, the EWF differs due to the different band gap. Also given are the calculated CNLs for a defect-free interface.[25,48]

further reduction of the VBO. At this point, the so-called doping limit according to the allowed doping range becomes important: In a previous study of La-doped HfO_2,[66] the nearly independent position of the Fermi level from the La doping concentration was attributed to the doping limit. Considering points (ii) to (iv), we assume an oxygen-poor condition at the TiN/HfO_2 interface. The energy range accessible for a shift of the Fermi level by doping in HfO_2 is extremely limited: Its lower boundary under oxygen-poor conditions is calculated to be about 3.5 eV above the VBM. Attempting to shift the Fermi level, and thus the VBO, below this value will lead to a spontaneous formation of additional defects for compensation. As depicted in Figure 5, the observed FL position of TiN in contact with undoped HfO_2 and HZO is already at the lower boundary of the doping range and a further decrease by cation doping is not expected.

4.2.3. Summary on TiN Electrodes

Considering the HfO_2 doping limit under oxygen-poor conditions, a conclusive picture of the observed VBOs at the TiN/HfO_2 interface can be obtained. The VBO variations can be related to the different interface defect concentrations in the different growth processes, with larger densities for PVD and smaller ones for ALD growth of HfO_2. The independence of the VBO on La and Gd doping can be explained by the fact that the TiN FL in the undoped case is already at the lower limit of the doping range and a further reduction by doping cannot be expected. Experimentally, we assume the lower limit of the doping range to be 3.3–3.4 eV above the VBM. In summary, the TiN/HfO_2 interface exhibits an intrinsically stable state with respect to the band alignment. The vacuum work function of TiN and the defect-free CNL of HfO_2 are nearly identical and both lie within the calculated doping range under oxygen-poor conditions. Oxygen vacancy defect states shift the CNL toward the CBM but keep it inside the doping range and allow for a proper band alignment. Even a change of the oxygen vacancy defect concentration, for example, by ferroelectric switching, keeps it within the doping range and allows compensation by proper band alignment.

For IrO_2 electrodes, the situation turns out to be completely different, as being discussed in the following.

4.3. Band Alignment for Ir and IrO_2 Electrodes

The chemistry of IrO_2 electrodes was extensively studied in previous publications.[7,56] Basically, IrO_2 electrodes remain chemically stable during annealing in oxide atmosphere (OA). In contrast, annealing in FGA (H_2:Ar, 20%:80%) leads to complete reduction of the IrO_2 top electrode to metallic Ir. However, the remaining Ir electrode contains a significant amount of dissolved but unbound oxygen.[64] The covered bottom electrode is not affected by the two annealing processes and remains stable as IrO_2. The different annealing processes thus allow the study of symmetric (IrO_2/HfO_2/IrO_2) and asymmetric (IrO_2/HfO_2/Ir) MFM structures grown under exactly the same preparation conditions. A TOF-SIMS analysis of the chemical composition reveals an oxygen enrichment, at least at the bottom electrode interface. Compared to TiN electrodes, ferroelectric cycling starts with a higher polarization in the pristine state and a less pronounced wake-up effect. The onset of fatigue, however, is already observed after

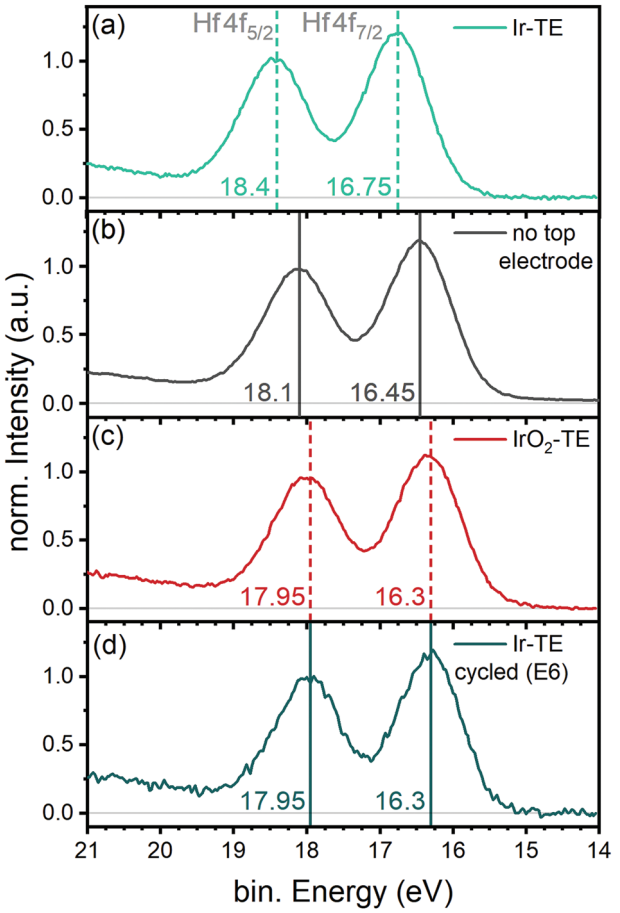

Figure 6. HAXPES Hf 4f core levels binding energy shifts for Ir and IrO_2 top electrodes from pristine samples. a) The Ir top electrode (FGA annealed) causes a rigid shift of 300 ± 50 meV toward higher binding energies, compared to b) the spectrum without top electrode (reference). c) The IrO_2 top electrode (oxygen annealed) causes a shift of 150 ± 50 meV toward lower binding energies. d) The Hf 4f spectrum of a sample with an Ir top electrode (FGA annealed) after 10^6 field cycles is shown, which now matches the spectrum of an IrO_2 top electrode sample.

about 10^6 switching cycles. Thus, an overall improvement compared to TiN electrodes could not be observed.

4.3.1. HAXPES Analysis of VBOs

Figure 6 shows the HAXPES Hf 4f spectra of samples with Ir or IrO_2 top electrode obtained either by (a), (d) FGA annealing or (c) oxygen annealing. In (b), a Hf 4f spectrum without top electrode is shown, which serves as a reference, in addition to the survey and valence band spectrum in Figure 3.

The HZO VBO without top electrode amounts 2.7 ± 0.05 eV and is associated with the band alignment at the bottom electrode. For the band alignment of the top electrode, the rigid binding energy shifts of the Hf 4f core levels as displayed in Figure 6a,c,d are considered. The VBOs of 3.0 and 2.55 eV are listed in Table 2 (samples 8 and 9).

Figure 6d shows an Hf 4f spectrum after 10^6 field cyclings, which matches the pristine spectrum of the IrO_2 electrode sample with a VBO of 2.55 eV, as displayed in Figure 6c. In contrast to the case of TiN, a Hf^{3+} component could not be clearly identified with the $Ir(O_2)$ electrodes. From these Hf 4f spectra and VBOs, listed in Table 2, four main points can be derived as essential information for Ir and IrO_2 electrodes:

(i) Although the vacuum work function of IrO_2 and TiN is almost the same, the VBO of IrO_2 electrodes is about 1 eV smaller.
(ii) In the Hf 4f spectra, no Hf^{3+} component is present as a signature of $V_O^{\bullet\bullet}$ vacancies.
(iii) The ferroelectric field cycling significantly changes the Ir band alignment of the top electrode and reverses the observed internal bias field.
(iv) Contrary to TiN electrodes, La doping of HfO_2 further reduces the VBO at IrO_2 electrodes (see sample 10 in Table 2).

Obviously, point (i) seemingly contradicts the FL pinning model, which was successfully applied in the previous section to derive the band alignment in the HfO_2 doping limit. At this point we recall the reason for studying IrO_2 electrodes: Due to its lower thermodynamic oxide stability compared to HfO_2[48] and experience from IrO_2/PZT-based capacitors,[67] IrO_2 was expected to act as an oxygen source to annihilate oxygen vacancies in HfO_2. Indeed, an oxygen-rich IrO_2 bottom electrode interface was recently observed by TOF-SIMS.[7] However, since the fatigue behavior of the samples deteriorates compared to TiN electrodes, the result contradicts the expectations.[7,56] As an explanation, we assume an exchange of oxygen at the interface leading to an oxygen-rich condition at the HfO_2 side of the interface.

In analogy to the shown band alignment of TiN electrodes in Figure 5, the experimentally observed band alignment for IrO_2 and Ir electrodes is depicted in **Figure 7**. However, as a consequence of the oxygen-rich condition of the HfO_2/HZO, the doping range is now shifted toward the VBM (compare Figure 2).

The shifted doping range prevents equivalent n-type band alignment of IrO_2 compared to TiN (see Figure 7a), since the IrO_2 FL must be placed within the allowed doping range. This downward shift of the IrO_2 FL also requires a significant downward shift of the CNL by the formation of negatively charged oxygen interstitials, as discussed in Section 2.3. Note, that the defect-free CNL, as depicted in Figure 7a, has to be shifted below the FL for a compensation of the potential step at the vacuum levels. Therefore, the band alignment is not intrinsically stable but has to be extrinsically stabilized by these oxygen interstitials. Consequently, if the number of interstitials at the interface is reduced in any way, new interstitial sites must be spontaneously formed to stabilize the band alignment, and the IrO_2 electrode acts as a source of oxygen. Because these interstitials are negatively charged, these defects are not indirectly detectable as Hf^{3+} component in the Hf 4f spectra, which explains point (ii).

Since the IrO_2 FL is near the upper boundary of the doping range, even a further reduction of the VBO by cation doping, as mentioned in (iv), is feasible, since a further downshift of the FL is possible within the allowed doping range.

For the Ir metal top electrode, the band alignment is depicted in Figure 7b. The observed VBO of 3.0 eV is nearly in line with the FL pinning model, assuming a defect-free CNL (see Table 3). Here, the doping range shifted toward the VBM by oxygen

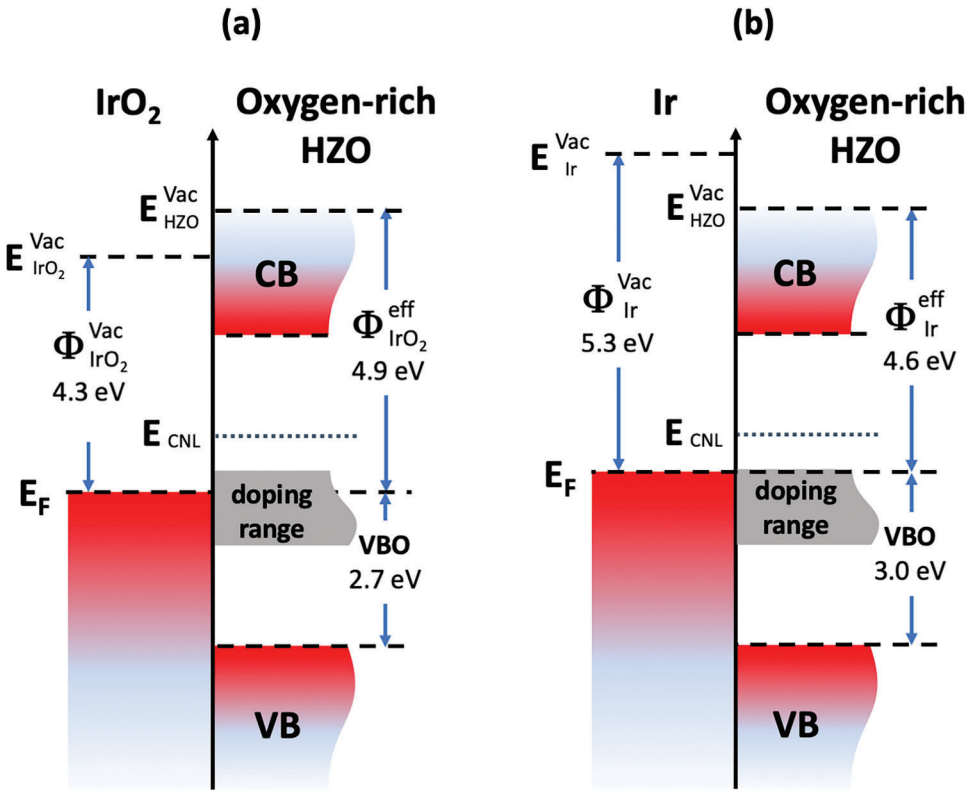

Figure 7. Schematic sketch of the IrO_2 (a) and Ir (b) band alignment with HZO. The charge neutrality level and doping limits under oxygen-rich conditions are given as calculated by Robertson et al.[25,48] The energy scale assumes a band gap of 5.4 eV and an electron affinity of 2.2 eV for HZO. The Ir and IrO_2 VBOs are experimentally observed.

enrichment supports a band alignment of a p-type metal such as Ir. For a proper band alignment according to the FL pinning Equation (5), only a minor adjustment of the CNL by additional negatively charged interstitial defects is required. However, this alignment requires an oxygen-rich condition at the HZO interface to shift the doping range to the correct position. Here, this is ensured by the deposition process, as the Ir top electrode results from a FGA reduction of previously deposited IrO_2.[56] Thus, these results must be distinguished from a direct deposition of Ir metal.

In comparison to $Ir(O_2)$ electrodes, a recently published study of $Ru(O_2)$ electrodes by Chernikova et al. is of particular importance.[8] Here, the same band alignment is observed for RuO_2 and Ru as was found for IrO_2 and Ir in this study. This contradicts the assumption that the FL band alignment depends on the metal vacuum work function since the vacuum work functions of IrO_2 and Ir are reversed compared to those of RuO_2 and Ru. Ir is a p-type metal with a vacuum work function of about 5.3 eV, comparable to RuO_2, while Ru is a n-type metal and has a vacuum work function of about 4.6 eV,[68] which is comparable to that of IrO_2. Nevertheless, the observed VBOs of Ir and Ru are identical and the VBOs of IrO_2 and RuO_2 as well, that is, although Ir and Ru have distinctly different vacuum work functions, their band alignment is the same, just as for IrO_2 and RuO_2 electrodes. Moreover, no Hf^{3+} signatures were observed within the Hf 4f spectra in either case. We conclude that the band alignment at IrO_2 and RuO_2 electrodes is not dependent on the respective vacuum work function but on the position of the doping range. The FL pinning equation is fulfilled by shifting the CNL due to oxygen interstitial defect charges—and not by adjusting the metal FL relative to a constant CNL.

In considering the VBO change due to ferroelectric cycling, as mentioned in point (iii) above, we will now examine the effects of ferroelectric cycling in more detail.

4.3.2. Impact of Ferroelectric Cycling

In **Figure 8**, the band alignment for pristine and cycled asymmetric $Ir/HfO_2/IrO_2$ capacitors is quantified and compared to a symmetric $IrO_2/HfO_2/IrO_2$ capacitor. The different VBOs at the top and bottom electrodes are determined from the Hf 4f core level shifts, as depicted in Figure 6. The different values of the VBOs for the bottom and top electrodes indicate an internal bias field (IB). For pristine $Ir/HfO_2/IrO_2$, the observed difference of −300 meV leads to a large IB field pointing toward the top electrode. After 10^6 cycles, the IB of the $Ir/HfO_2/IrO_2$ sample has changed to +150 meV, the same value as for the $IrO_2/HfO_2/IrO_2$ pristine sample. The internal bias fields manifest themselves as an inclined VBM and should be observable as the voltage bias of the J–V and P–V hysteresis loops. Thus, these spectroscopic results can directly relate cycle-dependent bias fields to the macroscopic ferroelectric properties of the MFM stacks.

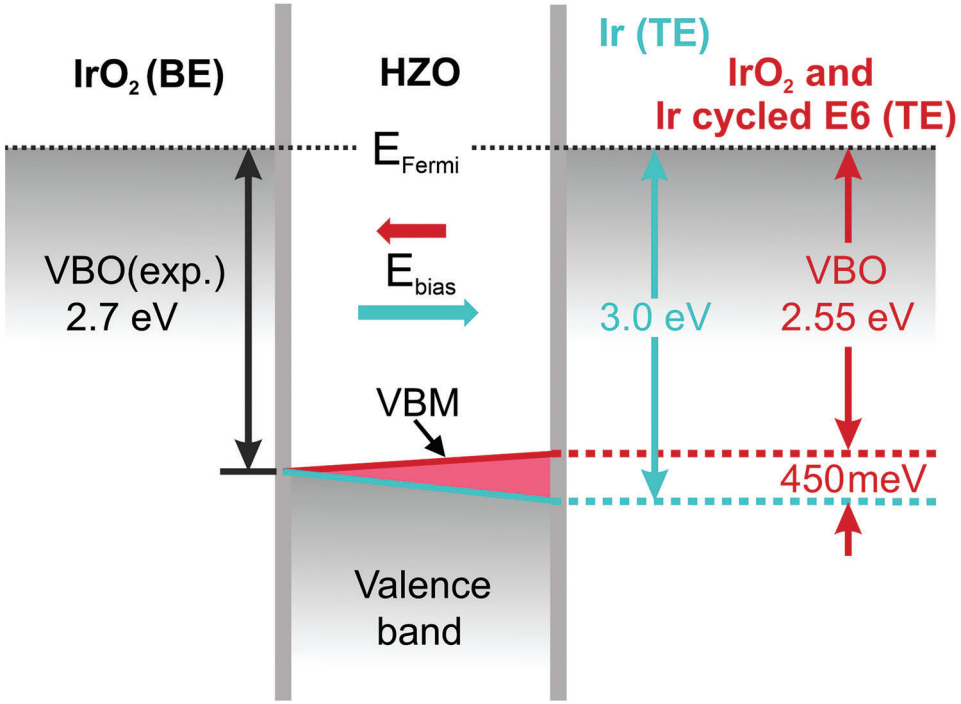

Figure 8. Band alignment between top and bottom electrode across ferroelectric HZO for different metal top electrodes (Ir, IrO_2) and number of ferroelectric switching cycles (10^0, 10^6)

Next, we determine the bias fields $\Delta E_c(N)$ dependent on the number of cycles N from the coercive fields of the respective J–V hysteresis curves as $\Delta E_c(N) = (E_c^+(N) + E_c^-(N))/2$. The results are shown in **Figure 9** for IrO_2/HZO/IrO_2 and Ir/HZO/IrO_2. The squared data points also indicate the Ir/HZO/IrO_2 cycles that relate to the HAXPES data in Figure 6.

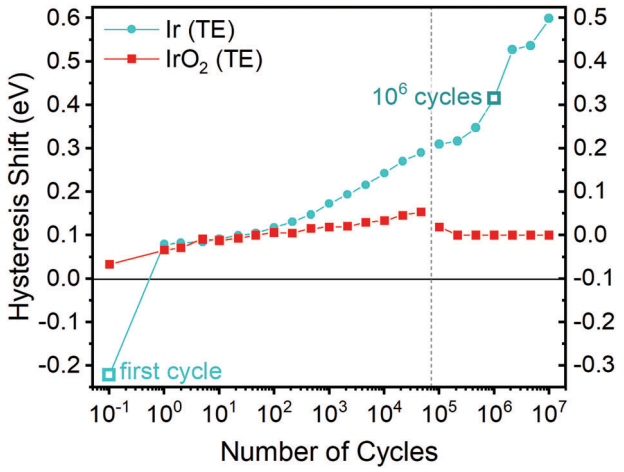

Figure 9. Hysteresis bias (HB) of Ir/HfO_2/IrO_2 and IrO_2/HfO_2/IrO_2 samples as a function of the number of switching cycles. Indicated by empty boxes are the values of the interface bias fields (IB) due to different VBOs at the top and bottom electrode interfaces. The right y-scale relates to data points $\geqslant 10^5$ cycling steps. They were shifted due to an experimental artifact, that occurred when switching to a different input channel at 10^5 cycling steps.

Depending on the cycling, the IrO_2/HZO/IrO_2 hysteresis bias (HB) shows a slightly increasing positive value, stabilizing at about +100 mV. In contrast, the Ir/HZO/IrO_2 sample shows a continuously increasing HB, starting from about −220 mV and going up to +450 mV after 10^6 cyclings. For the pristine samples, the IB field as observed by the HB agrees well with the VBO differences between bottom and top electrode as observed by HAXPES. This suggests that the observed macroscopic HB in the pristine state is mainly related to the microscopic interface properties, namely the different band alignments at the top and bottom electrodes. However, after 10^6 cyclings, the Ir/HZO/IrO_2 sample shows a significant difference between HB and IB. While the HB increases continuously, the IB from the band alignment shows the same value as for the IrO_2/HZO/IrO_2 sample. This indicates a cycle-dependent bias field component that is not related to different band alignments of the electrodes.

At this point, the interface chemistry of the Ir top electrode under ferroelectric cycling is inspected in more detail, in particular the O 1s emission. Due to the large information depth of the HAXPES experiment (≈20 nm), the O 1s spectrum contains contributions from both the oxide top electrode and the HZO layer underneath, revealing possible chemical interactions.

In order to track chemical interaction under ferroelectric cycling, **Figure 10** displays the O 1s core level along with the large Ir $4p_{3/2}$ emission measured on Ir/HZO/IrO_2 samples after 10^0 and 10^6 cycles, and along with an IrO_2 reference spectrum. The inelastic background and pure HZO contributions were subtracted from the raw data. The pure HZO component was determined from the reference sample without top electrode.

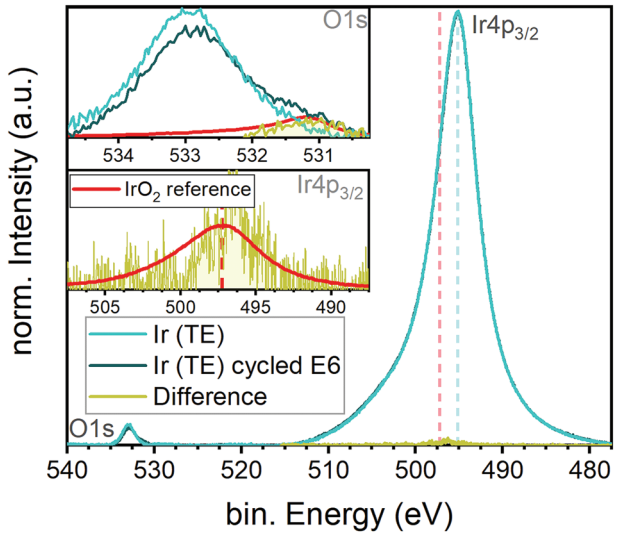

Figure 10. HAXPES spectra of the O 1s and Ir $4p_{3/2}$ core levels of forming gas annealed $IrO_2/HfO_2/Ir$ samples in the pristine state and after 10^6 switching cycles. The spectra are corrected for an inelastic background and for the HfO_2 contribution within the O 1s emission. Both spectra are normalized to the Ir 4p peak maximum. The insets show differences between pristine and a 10^6 times cycled sample. In both cases, the expected contribution from IrO_2, as determined from a reference sample, is indicated.

The inset of Figure 10 shows the enlarged O 1s region around $E_B \sim 533$ eV after 10^0 and 10^6 cycling conditions. The main component centered around $E_B = 533$ eV was identified as unbound oxygen in the Ir top electrode by Szyjka et al.[56] This oxygen component is most likely due to to hydroxide formation resulting from reduction of IrO_2 under FGA annealing. After 10^6 switching cycles, a general decrease in spectral intensity of this main component is observed, while on the other hand an additional component appears at ≈531 eV. The BE of this redistributed spectral component matches that of the IrO_2 component and appears for the 10^6 times cycled sample only. An IrO_2 reference peak is added as shaded area. As highlighted in the second inset of Figure 10, the metallic Ir $4p_{3/2}$ peak also shows a small intensity difference at the BE position of the IrO_2 component. In connection with the above discussion of the band alignment, it is worth noting that a peak appearing at the low binding energy side of the O 1s is often attributed to oxygen interstitials and a peak at the high binding energy side to oxygen vacancies.[64] Based on the simultaneous appearance of the additional IrO_2 intensity at the Ir $4p_{3/2}$ peak, we assume that the oxide component at 531 eV is, at least partly, due to IrO_2. However, an additional contribution from oxygen interstitials is possible.

Thus, we can clearly determine that a chemical reaction occurred when the sample was switched from 10^0 to 10^6. Obviously, the metallic Ir electrode oxidizes to IrO_2 directly at the HZO interface under repeated ferroelectric switching.

The formation of IrO_2 at the interface during cycling directly explains the observed band alignment of the cycled sample, which coincides with the $IrO_2/HZO/IrO_2$ (see Figure 6). Nevertheless, the formation of IrO_2 seems to be unexpected due to its lower thermodynamic stability compared to that of HfO_2. Here we can derive a possible explanation from the above band alignment model, considering in particular the role of oxygen interstitials.

As discussed in the previous section and sketched in **Figure 11**, the band alignment at the IrO_2 and Ir interfaces must be stabilized by negatively charged oxygen interstitials. Consequently, its density at the interfaces is strongly enhanced. It is known that ferroelectric cycling balances the distribution of defects due to their mobility under an applied electric field.[69] Therefore, for $IrO_2/HZO/IrO_2$ it is assumed that the oxygen interstitials from both electrodes are shifted into the HZO bulk (see Figure 11a). However, the resulting reduction at the interfaces must be immediately compensated by the formation of new interstitials in order to achieve a stable band alignment. In the end, cycling leads to a general increase in oxygen interstitials, which destabilizes the ferroelectric phase. At higher oxygen interstitial content, the m-phase is favored.[3]

For $Ir/HZO/IrO_2$, not only an imbalance of interstitials between the interfaces and the bulk is expected, but also between IrO_2 bottom electrode and the Ir top electrode since the Ir top electrode requires only a small amount of interstitials for a stable band alignment. The ferroelectric cycling leads to an increase of oxygen interstitials in the bulk and at the Ir top electrode interface. The increase of interstitials at the Ir interface is compensated by a downward shift of the FL (see Figure 7b). However, at a certain oxygen concentration, spontaneous formation of IrO_2 is expected to occur.[70]

4.3.3. Summary on Ir and IrO_2 Electrodes

The band alignment and ferroelectric cycling behavior of $Ir(O_2)$ electrodes can be consistently explained by assuming oxygen-rich electrode interfaces. From the above findings—including the rigid binding energy shifts of the Hf 4f, peaks as well as the evolution of the local interface chemistry derived from the O 1s emission—the following scenarios occurring at the HZO electrode interfaces are suggested:

- For IrO_2 electrodes, an oxygen exchange with HZO is assumed, leading to oxygen-rich condition at the HZO side of the interface. This leads to a shift of the HZO doping range toward the VBM and explains the significantly lower VBO compared to TiN electrodes since the FL is bound to the doping range. However, this band alignment must be extrinsically stabilized at the interface by a substantial amount of oxygen interstitials at the interface. This defect-stabilized band alignment is believed to be the reason for an unstable ferroelectric switching behavior as observed by a reduced remanent polarization during field cycling.
- For Ir electrode interfaces, an equivalent oxygen enrichment as for IrO_2 is assumed since Ir is obtained by a FGA reduction of a previously deposited IrO_2 electrode. The shifted doping range favors the band alignment of a p-type metal such as Ir, and only a small adjustment of the CNL associated with oxygen interstitials is required for a proper band alignment.
- Repeated switching successively equalizes the oxygen interstitials and attempts to homogenize the interstitial distribution. The resulting decrease at the IrO_2 interface must be compensated by the formation of new interstitial sites for a proper

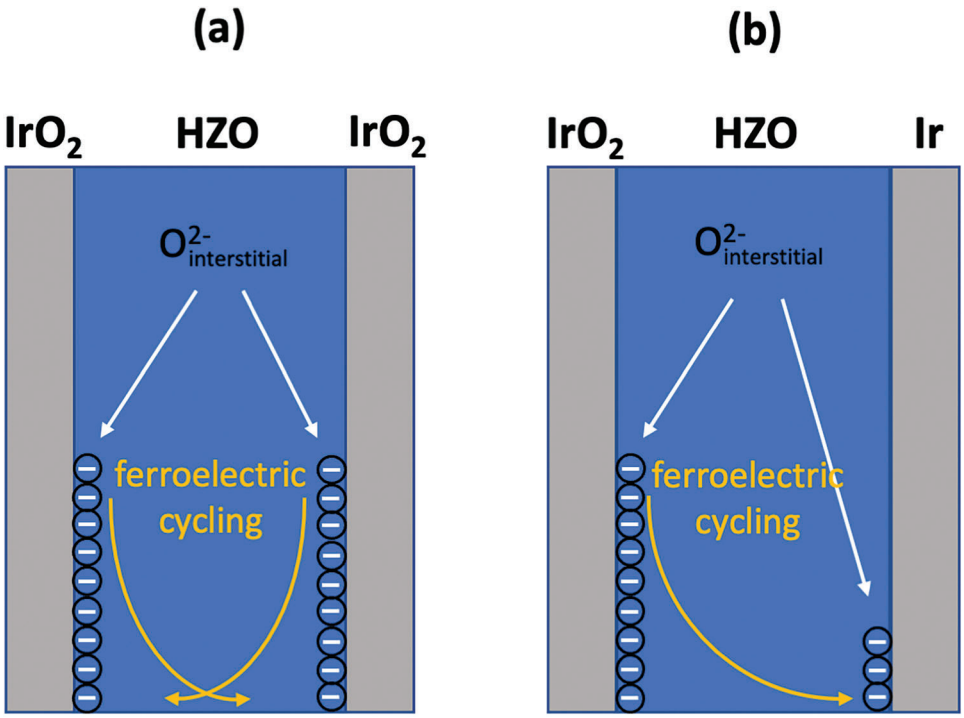

Figure 11. Effect of ferroelectric cycling on the distribution of oxygen interstitial defects for a) IrO_2/HZO/IrO_2 and b) IrO_2/HZO/Ir capacitors. The redistribution forces the continuous formation of new oxygen interstitials at the IrO_2 interface to stabilize the band alignment.

band alignment. The resulting increase at the Ir interface is compensated by an adjustment of the FL. At a certain oxygen concentration, spontaneous formation of an IrO_2 interface layer is expected. The overall increase of the oxygen interstitial concentration in the HZO layer during ferroelectric switching eventually destabilizes the ferroelectric phase of both the symmetric Ir(O_2)/HZO/IrO_2 and the asymmetric Ir/HZO/IrO_2 MFM stack, leading to early fatigue without breakdown.

5. General Summary

This study provides a novel view on the reliability issues of HfO_2-based FeCaps. As representatives for metal nitride and metal oxide electrodes, the interfacial band alignment has been analyzed for TiN/HZO/TiN and IrO_2/HZO/IrO_2 FeCaps using the FLP model, which in classical semiconductor physics properly describes metal/semiconductor band alignments.

Within the FLP model, we explicitly take into account i) the narrow doping limit of HfO_2 and ii) a chemical oxygen exchange at the metal/HZO interface, which has not been done before. As a result, the metallic FL is restricted to the narrow energy range of the doping limit, and its position depends on the oxygen concentration at the HfO_2 or HZO side of the interface. This is contrary to the classical M/SC case, where the metallic FL is freely adjustable within the band gap, without any restrictions by the doping limit. Thus, for M/HZO the band alignment is not set by the FL adjustment of the metal—but by the positioning of the CNL of the HZO by defects, since the FL is pinned by the doping range, which, in turn, depends on the interface oxygen concentration. We qualitatively discussed oxygen-poor and oxygen-rich conditions at the HZO interface, which serve as two extreme cases of the general case of a FE/metal interface. As a consequence, the possible doping range shifts from a position near the conduction band for oxygen-poor interfaces toward the valence band for oxygen-rich conditions.[15,25] The size and the position of the limited doping energy range within the gap turns out to be of crucial importance for the band alignment and the oxygen defect density at the electrode interfaces. The TiN(TaN)/HZO interface is considered as oxygen-poor due to the well-known oxygen scavenging from HfO_2.[16] The IrO_2/HZO interface is considered to be oxygen rich; the oxygen supply originates from the electrode itself as it is chemically unstable compared to HfO_2 and HZO.[7,56]

For TiN and TaN electrodes the resulting possible doping range in HfO_2 fits to the required range for a band alignment of the TiN FL. The alignment with respect to the CNL within the FLP model can be achieved nearly independent of the actual oxygen vacancy defect density at the interface. Thus the band alignment at the TiN interface may be viewed as intrinsically stable and a possible change of the defect density at the interface by ferroelectric cycling does not affect the band alignment.

In contrast, the oxygen-rich condition at the IrO_2 interface shifts the possible doping range toward the valence band and out of the required range for an intrinsically stable band alignment of IrO_2. The alignment has to be extrinsically stabilized by defects, in this case oxygen interstitials. In terms of the FLP-model this means that the CNL has to be shifted by interface defect states for a proper alignment, whereas the IrO_2 FL is bound to the energy position of the doping range. This view is supported by a recent investigation of RuO_2 electrodes.[8] It shows the same band alignment, although its vacuum work function is p-like, contrary to the n-like IrO_2. Thus, in both cases, IrO_2 and RuO_2, we assume a "pinning" of the FL to the oxygen-rich doping range. The

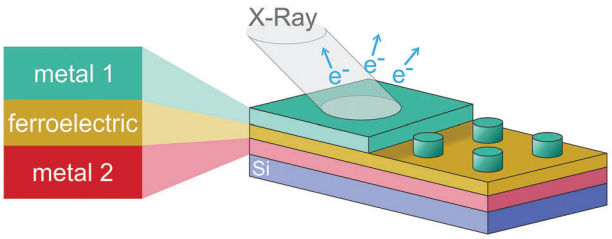

Figure 12. Schematics of the ferroelectric sample stacks investigated both, by HAXPES and electric field cycling experiments. The structured top electrode in general consists of differently sized dots for ferroelectric cycling as well as a several 100µm large area for X-ray diffraction experiments. HAXPES was performed on this planar area (left part of the sample) as well as on the structured dots. The bottom electrode was accessible from the areas in between the dots.

band alignment is achieved by a shift of the CNL due to oxygen interstitial defects.

For the Ir electrode also an oxygen-rich interface is assumed due to the electrode creation by a reduction of IrO_2 with FGA. In this case the oxygen-rich doping range supports the alignment of a p-like metal like Ir and only a small shift of the CNL by oxygen interstitials has to be assumed. Nevertheless an oxygen-rich interface has to be created for the alignment of a p-like metal. Therefore, an Ir electrode originating from a reduced IrO_2 layer, behaves different from directly deposited Ir metal. In general, for electrodes, which neither supply nor scavenge oxygen, like W, Pt, or even TiO_2, the defect creation at the interface strongly depends on the conditions of the growth process[64,71]

The field cycling-induced reduction of the FE polarization in $Ir(O_2)/HfO_2$-based capacitors is explained by the mobility of oxygen interstitials under an applied electric field. Since interstitial oxygen defects are mandatory for a stable band alignment, a reduction at the interface by ferroelectric cycling destabilizes the alignment and new interstitials have to be created. Thus, the continuously increased interstitial concentration during cycling favors the transition of the FE orthorhombic to the non-FE monoclinic phase.

As a general rule, n-type metals at an oxygen-poor interface and p-type metals at an oxygen-rich interface may be considered as stable electrodes, whereas n-type metals at an oxygen-rich and p-type metals at an oxygen-poor interface require a significant amount of oxygen vacancies or interstitials for a stable band alignment.

6. Experimental Section

Our general sample structure, as given in **Figure 12** allowed a combined analysis by HAXPES, tranport measurements, and X-ray diffraction for structural analysis of the same sample. The X-ray spot size allowed a selected HAXPES analysis from all individual sample areas, whereas ferroelectric hysteresis measurements were obtained from the dots and the large area was used for an X-ray diffraction analysis of the crystal structure.

In this work, MIM structures were investigated both by HAXPES and electrical measurements with the general layout of the samples shown in Figure 12. An $IrO_2/HZO/IrO_2$ sample stack was grown on a boron-doped Si substrate. The nominal 10 nm IrO_2 bottom and 20 nm IrO_2 top electrodes were deposited by sputtering from a pure Ir target with process gas of a 20:5 sccm $Ar:O_2$ ratio.

The TiN/(HfO_2,HZO)/TiN trilayer structures were grown onto silicon substrates; each of the layers has a thickness of 10 nm. The bottom and top TiN electrodes were deposited by physical vapour deposition (PVD) at a base pressure of $p = 10^{-9}$ mbar. The Ti target was sputtered in 20 sccm Ar and 4 sccm N_2 flow, respectively. For the deposition of the ferroelectric HfO_2 and HZO layer we applied PVD and ALD. The HfO_2 film deposition by PVD was accomplished in the same chamber as the TiN electrodes without breaking the vacuum. The ALD samples, in contrast, experienced ambient conditions before and after HfO_2 deposition in another chamber In the PVD process, a ceramic HfO_2 target with 99.9 % purity was sputtered in an oxygen backpressure of 1.2×10^{-3} mbar at room temperature.

In the ALD process, HfO_2 was grown layer-by-layer by cyclically exposing a metal–organic precursor (TEMA-Hf; $[(CH_3)(C_2H_5)N]_4Hf$) to reactive ozone (O_3), which served as the oxygen source. The process temperature was set to 250 °C and the oxygen supply was controlled by applying different ozone pulse times, 10 and 60 s, respectively, whereas the TEMA-Hf was supplied for 2 s. After 100 cycles, the HfO_2 thickness amounted to 10 nm. The $Hf_{0.5}Zr_{0.5}O_2$ (HZO) film was prepared by ALD at 250 °C substrate temperature with $Hf[N(CH_3)(C_2H_5)]_4$ and $CpZr[N(CH_3)_2]_3$ precursors as Hf and Zr sources. Oxygen plasma was used as an oxidant.

The IrO_2 top electrodes were sputtered through a shadow mask with an array of dots with diameters ranging from 110 to 450 µm, and an additional ≈1 cm wide window for structural X-ray characterization. This sample was split into equal parts to undergo different crystallization anneal steps for each sample. Thus, apart from the crystallization annealing, all samples were equivalent. Annealing was performed in a rapid thermal processing tool in oxygen (OA) for 60 s, or in FGA ambient (FG, 9:1 $N_2:H_2$ ratio) for 20 s. An annealing temperature of 500 °C was used since IrO_2 was known to be thermally unstable even above 200 °C.[72] Further experimental details on sample characterization and electrical measurements are published by Materano et al.[3] and Mittmann et al.[7]

HAXPES was performed at the P22 beamline of PETRA III (DESY, Hamburg)[73] to investigate element-selective and depth-dependent chemical properties and band alignment. Core level spectra of Hf, Zr, Ir, and O were recorded at a photon energy of 6 keV. HAXPES thereby provided a large information depth of about 20 nm to probe at least the HZO layer together with the top electrode of the capacitor stack collectively.[74,75]

Acknowledgements

This project has received funding from the European Union's Horizon 2020 research and innovation programme under grant agreement No 780302. The authors acknowledge DESY (Hamburg, Germany), a member of the Helmholtz Association HGF, for the provision of experimental facilities, in particular beamline P22. This work has also received funding from the BMBF (project 05K22VL1), by University of Konstanz BlueSky initiative, and by the VECTOR Foundation (project iOSMEMO). Funding for the HAXPES instrument at beamline P22 by the Federal Ministry of Education and Research (BMBF) under contracts 05KS7UM1 and 05K10UMA with Universität Mainz; 05KS7WW3, 05K10WW1, and 05K13WW1 with Universität Würzburg is gratefully acknowledged. Parts of this work was financially supported out of the state budget approved by the delegates of the Saxon State parliament.

Open access funding enabled and organized by Projekt DEAL.

Conflict of Interest

The authors declare no conflict of interest.

Data Availability Statement

The data that support the findings of this study are available from the corresponding author upon reasonable request.

Keywords

band alignment, fatigue, ferroelectrics, hard X-ray photoelectron spectroscopy, HfO_2, interstitials, vacancies

Received: June 23, 2023
Revised: August 16, 2023
Published online: October 8, 2023

[1] H. Kohlstedt, Y. Mustafa, A. Gerber, A. Petraru, M. Fitsilis, R. Meyer, U. Böttger, R. Waser, *Microelectron. Eng.* **2005**, *80*, 296, 14th biennial Conference on Insulating Films on Semiconductors.
[2] J. Müller, T. S. Böscke, D. Bräuhaus, U. Schröder, U. Böttger, J. Sundqvist, P. Kücher, T. Mikolajick, L. Frey, *Appl. Phys. Lett.* **2011**, *99*, 112901.
[3] M. Materano, C. Richter, T. Mikolajick, U. Schroeder, *J. Vac. Sci. Technol. A* **2020**, *38*, 022402.
[4] F. P. G. Fengler, M. Pešić, S. Starschich, T. Schneller, U. Böttger, T. Schenk, M. H. Park, T. Mikolajick, U. Schroeder, in *2016 46th European Solid-State Device Research Conference (ESSDERC)*, **2016**, pp. 369–372.
[5] M. H. Park, Y. H. Lee, T. Mikolajick, U. Schroeder, C. S. Hwang, *MRS Commun.* **2018**, *8*, 795.
[6] D. H. Lee, Y. Lee, Y. H. Cho, H. Choi, S. H. Kim, M. H. Park, *Adv. Funct. Mater.* **2023**, 2303956.
[7] T. Mittmann, T. Szyjka, H. Alex, M. C. Istrate, P. D. Lomenzo, L. Baumgarten, M. Müller, J. L. Jones, L. Pintilie, T. Mikolajick, U. Schroeder, *Phys. Status Solidi RRL* **2021**, *15*, 2100012.
[8] A. G. Chernikova, Y. Y. Lebedinskii, R. R. Khakimov, A. M. Markeev, *Appl. Phys. Lett.* **2023**, *122*, 021601.
[9] R. Alcala, M. Materano, P. D. Lomenzo, P. Vishnumurthy, W. Hamouda, C. Dubourdieu, A. Kersch, N. Barrett, T. Mikolajick, U. Schroeder, *Adv. Funct. Mater.* **2023**, 2303261.
[10] M. Materano, P. D. Lomenzo, A. Kersch, M. H. Park, T. Mikolajick, U. Schroeder, *Inorg. Chem. Front.* **2021**, *8*, 2650.
[11] Y. Zhang, Y. Y. Shao, X. B. Lu, M. Zeng, Z. Zhang, X. S. Gao, X. J. Zhang, J.-M. Liu, J. Y. Dai, *Appl. Phys. Lett.* **2014**, *105*, 172902.
[12] T. Mittmann, M. Materano, P. D. Lomenzo, M. H. Park, I. Stolichnov, M. Cavalieri, C. Zhou, C.-C. Chung, J. L. Jones, T. Szyjka, M. Müller, A. Kersch, T. Mikolajick, U. Schroeder, *Adv. Mater. Interfaces* **2019**, *6*, 1900042.
[13] M. H. Park, D. H. Lee, K. Yang, J.-Y. Park, G. T. Yu, H. W. Park, M. Materano, T. Mittmann, P. D. Lomenzo, T. Mikolajick, U. Schroeder, C. S. Hwang, *J. Mater. Chem. C* (**2020**), *8*, 10526.
[14] K. McKenna, A. Shluger, V. Iglesias, M. Porti, M. Nafría, M. Lanza, G. Bersuker, *Microelectron. Eng.* **2011**, *88*, 1272, proceedings of the 17th Biennial International Insulating Films on Semiconductor Conference.
[15] J. Wei, L. Jiang, M. Huang, Y. Wu, S. Chen, *Adv. Funct. Mater.* **2021**, *31*, 2104913.
[16] W. Hamouda, A. Pancotti, C. Lubin, L. Tortech, C. Richter, T. Mikolajick, U. Schroeder, N. Barrett, *J. Appl. Phys.* **2020**, *127*, 064105.
[17] A. K. Tagantsev, I. Stolichnov, E. L. Colla, N. Setter, *J. Appl. Phys.* **2001**, *90*, 1387.
[18] J. Rodriguez, K. Remack, K. Boku, K. Udayakumar, S. Aggarwal, S. Summerfelt, F. Celii, S. Martin, L. Hall, K. Taylor, T. Moise, H. McAdams, J. McPherson, R. Bailey, G. Fox, M. Depner, *IEEE Trans. Device Mater. Reliab.* **2004**, *4*, 436.
[19] J. Bardeen, *Phys. Rev.* **1947**, *71*, 717.
[20] A. M. Cowley, S. M. Sze, *J. Appl. Phys.* **1965**, *36*, 3212.
[21] W. Mönch, *Electronic Properties of Semiconductor Interfaces*, vol. *43*, Springer-Verlag, Berlin **2004**.
[22] J. Robertson, *J. Vac. Sci. Technol.* **2000**, *18*, 1785.
[23] G. D. Wilk, R. M. Wallace, J. M. Anthony, *J. Appl. Phys.* **2001**, *89*, 5243.
[24] B. Max, M. Pešić, S. Slesazeck, T. Mikolajick, *J. Appl. Phys.* **2018**, *123*, 134102.
[25] J. Robertson, S. J. Clark, *Phys. Rev. B* **2011**, *83*, 075205.
[26] M. Müller, P. Lömker, P. Rosenberger, M. Hussein Hamed, D. N. Mueller, R. A. Heinen, T. Szyjka, L. Baumgarten, *J. Vac. Sci. Technol. A* **2022**, *40*, 013215.
[27] C. Kalha, N. K. Fernando, P. Bhatt, F. O. L. Johansson, A. Lindblad, H. Rensmo, L. Z. Medina, R. Lindblad, S. Siol, L. P. H. Jeurgens, C. Cancellieri, K. Rossnagel, K. Medjanik, G. Schönhense, M. Simon, A. X. Gray, S. Nemšák, P. Lömker, C. Schlueter, A. Regoutz, *J. Phys.: Condens. Matter* **2021**, *33*, 233001.
[28] D. R. Islamov, V. A. Gritsenko, T. V. Perevalov, V. A. Pustovarov, O. M. Orlov, A. G. Chernikova, A. M. Markeev, S. Slesazeck, U. Schroeder, T. Mikolajick, G. Y. Krasnikov, *Acta Mater.* **2019**, *166*, 47.
[29] W. Mönch, *J. Vac. Sci. Technol.* **1996**, *14*, 2985.
[30] J. Robertson, *J. Vac. Sci. Technol. A* **2013**, *31*, 050821.
[31] M. A. Jenkins, K. E. K. Holden, S. W. Smith, M. T. Brumbach, M. D. Henry, C. Weiland, J. C. Woicik, S. T. Jaszewski, J. F. Ihlefeld, J. F. Conley, *ACS Appl. Mater. Interfaces* **2021**, *13*, 14634.
[32] D. H. Triyoso, R. I. Hegde, J. K. Schaeffer, R. Gregory, X.-D. Wang, M. Canonico, D. Roan, E. A. Hebert, K. Kim, J. Jiang, R. Rai, V. Kaushik, S. B. Samavedam, N. Rochat, *J. Vac. Sci. Technol.* **2007**, *25*, 845.
[33] D.-Y. Cho, H.-S. Jung, C. S. Hwang, *Phys. Rev. B* **2010**, *82*, 094104.
[34] T. E. Cook, C. C. Fulton, W. J. Mecouch, R. F. Davis, G. Lucovsky, R. J. Nemanich, *J. Appl. Phys.* **2003**, *94*, 7155.
[35] E. Bersch, S. Rangan, R. A. Bartynski, E. Garfunkel, E. Vescovo, *Phys. Rev. B* **2008**, *78*, 085114.
[36] Z. Q. Liu, W. K. Chim, S. Y. Chiam, J. S. Pan, C. M. Ng, *J. Mater. Chem.* **2012**, *22*, 17887.
[37] Y. Peng, G. Han, W. Xiao, Y. Liu, Q. Li, C. Zhang, J. Zhang, Y. Hao, *Superlattices Microstruct.* **2019**, *130*, 519.
[38] F. Ambriz-Vargas, G. Kolhatkar, R. Thomas, R. Nouar, A. Sarkissian, C. Gomez-Yáñez, M. A. Gauthier, A. Ruediger, *Appl. Phys. Lett.* **2017**, *110*, 093106.
[39] T. V. Perevalov, A. A. Gismatulin, V. A. Gritsenko, I. P. Prosvirin, F. Mehmood, T. Mikolajick, U. Schroeder, *Appl. Phys. Lett.* **2021**, *118*, 262903.
[40] T. Perevalov, V. Gritsenko, D. Islamov, I. Prosvirin, *JETP Lett.* **2018**, *107*, 55.
[41] S. A. Corrêa, S. Brizzi, D. Schmeisser, *ECS Trans.* **2016**, *75*, 145.
[42] Y.-C. Yeo, P. Ranade, T.-J. King, C. Hu, *IEEE Electron Device Lett.* **2002**, *23*, 342.
[43] D. Gu, S. K. Dey, P. Majhi, *Appl. Phys. Lett.* **2006**, *89*, 082907.
[44] K. Xiong, J. Robertson, M. C. Gibson, S. J. Clark, *Appl. Phys. Lett.* **2005**, *87*, 183505.
[45] J. L. Gavartin, D. M. Ramo, A. L. Shluger, G. Bersuker, B. H. Lee, *Appl. Phys. Lett.* **2006**, *89*, 082908.
[46] H. Takeuchi, D. Ha, T.-J. King, *J. Vac. Sci. Technol. A* **2004**, *22*, 1337.
[47] P. Broqvist, A. Pasquarello, *Appl. Phys. Lett.* **2006**, *89*, 262904.
[48] J. Robertson, Z. Zhang, *MRS Bull.* **2021**, *46*, 1037.
[49] S. B. Zhang, *J. Phys.: Condens. Matter* **2002**, *14*, R881.
[50] J. X. Zheng, G. Ceder, T. Maxisch, W. K. Chim, W. K. Choi, *Phys. Rev. B* **2007**, *75*, 104112.
[51] S. Clark, L. Lin, J. Robertson, *Microelectron. Eng.* **2011**, *88*, 1464, proceedings of the 17th Biennial International Insulating Films on Semiconductor Conference.
[52] M. N. K. Alam, S. Clima, B. J. O'Sullivan, B. Kaczer, G. Pourtois, M. Heyns, J. Van Houdt, *J. Appl. Phys.* **2021**, *129*, 084102.
[53] R. T. Tung, *Appl. Phys. Rev.* **2014**, *1*, 011304.
[54] S. Tanuma, C. J. Powell, D. R. Penn, *Surf. Interface Anal.* **2011**, *43*, 689.
[55] E. A. Kraut, R. W. Grant, J. R. Waldrop, S. P. Kowalczyk, *Phys. Rev. Lett.* **1980**, *44*, 1620.

[56] T. Szyjka, L. Baumgarten, T. Mittmann, Y. Matveyev, C. Schlueter, T. Mikolajick, U. Schroeder, M. Müller, *Phys. Status Solidi* **2021**, *15*, 2100027.
[57] R. G. Wilson, *J. Appl. Phys.* **1966**, *37*, 3170.
[58] G. N. Derry, M. E. Kern, E. H. Worth, *J. Vac. Sci. Technol. A* **2015**, *33*, 060801.
[59] B. R. Chalamala, Y. Wei, R. H. Reuss, S. Aggarwal, B. E. Gnade, R. Ramesh, J. M. Bernhard, E. D. Sosa, D. E. Golden, *Appl. Phys. Lett.* **1999**, *74*, 1394.
[60] J. K. Schaeffer, C. Capasso, L. R. C. Fonseca, S. Samavedam, D. C. Gilmer, Y. Liang, S. Kalpat, B. Adetutu, H. Tseng, Y. Shiho, A. Demkov, R. Hegde, W. J. Taylor, R. Gregory, J. Jiang, E. Luckowski, M. V. Raymond, K. Moore, D. Triyoso, D. Roan, B. E. White Jr, P. J. Tobin, in *IEDM Technical Digest. IEEE International Electron Devices Meeting*, **2004**, pp. 287–290.
[61] L. Lima, J. Diniz, I. Doi, J. Godoy Fo, *Microelectron. Eng.* **2012**, *92*, 86, 27th Annual Advanced Metallization Conference 2010.
[62] T. Szyjka, L. Baumgarten, T. Mittmann, Y. Matveyev, C. Schlueter, T. Mikolajick, U. Schroeder, M. Müller, *ACS Appl. Electron. Mater.* **2020**, *2*, 3152.
[63] F. Mehmood, R. Alcala, P. Vishnumurthy, B. Xu, R. Sachdeva, T. Mikolajick, U. Schroeder, *Adv. Mater. Interfac* **2023**, *10*, 2202151.
[64] L. Baumgarten, T. Szyjka, T. Mittmann, M. Materano, Y. Matveyev, C. Schlueter, T. Mikolajick, U. Schroeder, M. Müller, *Appl. Phys. Lett.* **2021**, *118*, 032903.
[65] R. Materlik, C. Künneth, M. Falkowski, T. Mikolajick, A. Kersch, *J. Appl. Phys.* **2018**, *123*, 164101.
[66] T. Szyjka, L. Baumgarten, O. Rehm, C. Richter, Y. Matveyev, C. Schlueter, T. Mikolajick, U. Schroeder, M. Müller, *Phys. Status Solidi* **2022**, *16*, 2100582.
[67] H. Fujisawa, S. Hyodo, K. Jitsui, M. Shimizu, H. Niu, H. Okino, T. Shiosaki, *Integr. Ferroelectr.* **1998**, *21*, 107.
[68] M. Ťapajna, K. Hušeková, J. Espinos, L. Harmatha, K. Fröhlich, *Materials Science in Semiconductor Processing* **2006**, *9*, 969, e-MRS 2006 Spring Meeting - Symposium L: Characterization of high-k dielectric materials.
[69] M. Pešić, F. P. G. Fengler, L. Larcher, A. Padovani, T. Schenk, E. D. Grimley, X. Sang, J. M. LeBeau, S. Slesazeck, U. Schroeder, T. Mikolajick, *Adv. Funct. Mater.* **2016**, *26*, 4601.
[70] Z. Novotny, B. Tobler, L. Artiglia, M. Fischer, M. Schreck, J. Raabe, J. Osterwalder, *J. Phys. Chem. Lett.* **2020**, *11*, 3601.
[71] M. Materano, T. Mittmann, P. D. Lomenzo, C. Zhou, J. L. Jones, M. Falkowski, A. Kersch, T. Mikolajick, U. Schroeder, *ACS Appl. Electron. Mater.* **2020**, *2*, 3618.
[72] M. J. Heikkilä, J. Hämäläinen, E. Puukilainen, M. Leskelä, M. Ritala, *J. Appl. Crystallogr.* **2020**, *53*, 369.
[73] C. Schlueter, A. Gloskovskii, K. Ederer, I. Schostak, S. Piec, I. Sarkar, Y. Matveyev, P. Lömker, M. Sing, R. Claessen, C. Wiemann, C. M. Schneider, K. Medjanik, G. Schönhense, P. Amann, A. Nilsson, W. Drube, S. Gwo, D.-J. Huang, D.-H. Wei, *AIP Conf. Proc.* **2019**, *2054*, 040010.
[74] M. H. Hamed, R. A. Hinz, P. Lömker, M. Wilhelm, A. Gloskovskii, P. Bencok, C. Schmitz-Antoniak, H. Elnaggar, C. M. Schneider, M. Müller, *ACS Appl. Mater. Interfaces* **2019**, *11*, 7576.
[75] C. Caspers, A. Gloskovskii, M. Gorgoi, C. Besson, M. Luysberg, K. Rushchanskii, M. Ležaić, C. S. Fadley, W. Drube, M. Müller, *Sci. Rep.* **2016**, *6*, 22912.